

FINDING X-RAY CORONAL CYCLES IN LOW MASS STARS¹

MAURICE WILSON^{2,3}, HANS M. GÜNTHER², AND KATIE AUCHETTL²

August 10, 2014

ABSTRACT

For this research, we intend to verify whether or not 9 stellar sources exhibit magnetic activity cycles via X-ray emission from coronae. The Sun is our most convenient source of information on how the magnetic activity increases over the course of a stellar cycle. Understanding features of the solar dynamo, such as flares and sunspots, is useful when searching for cycles on other stars. Flares can dramatically increase the flux of stars for short times and, in observations with insufficient time coverage, can be confused for the maximum of the stars' magnetic cycles (if they have one). In this analysis, we have discarded times where solar proton flares are detected in the data. The 9 stars we analyze were observed on a time scale of ~ 11 years by *Chandra* and *XMM Newton*. All of these stars lie in the Chandra Deep Field South. We utilize an APEC model that accounts for an optically thin coronal plasma environment to fit our stellar spectra. Because our sources are faint, we do not subtract the background, instead we find a satisfactory model to fit the background and the source spectra at the same time. We use χ^2 statistics to determine the confidence of our fits. We have light curves for the four brightest sources and determine that sources are too faint to conclusively state that the flux of one remains constant throughout all epochs or that one experiences a periodic long-term X-ray coronal cycle.

Subject headings: stars: activity - star: coronae - X-rays: stars

1. INTRODUCTION

Over a century ago, Heinrich Schwabe observed sunspots for 17 years and proposed a 10-year sunspot cycle (Schwabe 1843). This work led George Hale to discern that the solar magnetic field flips on average every 11 years. He recognized more spectral transition lines than initially expected while analyzing the Sun. When an active region on the Sun was observed, he noticed his spectra had more absorption lines within a very small energy range where there is typically only one. This is known as Zeeman Splitting and was discovered in 1897. This effect allowed him to infer the existence of magnetic fields in sunspots (Hale 1908). Since then, physicists have been successful in utilizing Ca II H and K emission lines to find activity cycles in the chromospheres of many other stars. The results from the chromosphere helped confirm that the following four stars undergo long-term X-ray coronal cycles as well: 61 Cygni A (Hempelmann et al. 2006), HD 81809 (Favata et al. 2008), α Centauri B (Robrade et al. 2005; Ayres et al. 2008; Ayres 2009), and the Sun. The revelation of the four stellar X-ray cycles is largely due to O.C. Wilson defining what is known as the S-Index. The S-Index expresses the ratio of the intensity of the chromospheric emission lines to the star's photospheric continuum (Wilson 1968). The spectral information gathered from the four stars have persuaded scientists that solar-type main-sequence stars are good candidates for exhibiting magnetic cycles (Wilson 1978; Baliunas et al. 1995).

¹ Based on observations obtained with XMM-Newton, an ESA science mission with instruments and contributions directly funded by ESA Member States and NASA

² Harvard-Smithsonian Center for Astrophysics, 60 Garden Street, Cambridge, MA 02138, USA

³ Department of Physics, Embry-Riddle Aeronautical University, 600 South Clyde Morris Boulevard, Daytona Beach, FL 32114, USA; WilsoM26@my.erau.edu

In regards to the solar cycle, the dynamo has yet to be thoroughly understood. In order for a model to plausibly represent the solar dynamo it must explain how the Sun's flowing magnetized fluids can sustain the cyclic regeneration of the magnetic field that has been observed. Charbonneau (2010) stated that a good solar dynamo model must also include the following characteristics:

- cyclic polarity reversals with a 10 yr half-period
- equatorward migration of the sunspot-generating deep toroidal field and its inferred strength
- poleward migration of the diffuse surface field
- polar field strength
- predominantly negative (positive) magnetic helicity in the Northern (Southern) solar hemisphere.

According to the general consensus, the solar magnetic/sunspot cycle starts from an energetic $\alpha - \Omega$ dynamo, which is created in the convective envelope of the star as the plasma transports energy towards the photosphere and corona. This process and following explanation are illustrated in Figure 1. (a) Initially, the solar field is poloidal in structure. (b) Subsequently, differential rotation evolves this into a toroidal field. This is known as the Omega effect. (c) In the convection zone, a flux rope of magnetized fluid decreases in density due to the balancing of internal and external pressures. Consequently, buoyancy occurs and the unstable flux rope emerges toward the photosphere and corona. (d) Simultaneously, these magnetic structures expand and spin due to force from the Coriolis effect. This phenomenon is known as the Alpha effect. (e) Flux ropes make up the horizontal component of the solar magnetic field. (f) This may contribute to the reborn, reversed poloidal field

that is produced at the commencement of a new sunspot cycle and at the halfway mark of a magnetic cycle (Charbonneau 2010).

The feasibility of detecting periodicities of magnetic activity in stars differs depending on which energy band is observed. Thus far, stellar UV emission has proven to be the most convenient medium for detecting magnetic flux variability over long time scales. Simply put, ground based telescopes can easily detect the UV band from stars and this allows us to observe the Ca II H and K emission lines that have provided conclusive evidence for the existence of stellar magnetic cycles in stars other than our Sun (Baliunas et al. 1995). Unfortunately, X-ray observatories must operate above the Earth’s atmosphere since X-rays are thoroughly absorbed before reaching the Earth’s surface. Consequently, there have been more observation projects observing stars in the UV bands.

X-ray observations have been important when searching for activity cycles because this energy range conveys coronal activity information from stars. In main-sequence stars, coronae contain the active regions where charged plasma follow magnetic field lines. Active regions are typically above a pair of sunspots in the photosphere (Charbonneau 2010). Because active regions from distant stars provide magnetic cycle information, instruments used for detecting magnetic activity periodicities should be capable of detecting variability without the aid of the photosphere’s sunspots. Notable active region and sunspot behaviors are displayed in Figures 2 and 3. Figure 2 illustrates the migration of active regions. Figure 3 shows the cyclic migration of sunspots and the fractional area of the hemisphere covered by sunspots.

In Section 2, we discuss the data reduction process and our methods used in this analysis. In Section 3 we explain our evaluations inferred from the resultant light curves. In Section 4 we end with our conclusions.

2. OBSERVATIONS AND DATA ANALYSIS

In this analysis, nine stars, that have been observed repeatedly by *Chandra* and *XMM-Newton*, are analyzed as potential candidates for detecting cyclic variability in their magnetic activities. These nine were chosen because they all are in the Chandra Deep Field South (CDFS). *Chandra* and *XMM-Newton* have observed them frequently for over a decade. This field is primarily observed for studying galaxies. However, there are stellar point sources seen near the edge of this field. Although these point sources are faint, both X-ray observatories have gathered plenty of data over the years since their missions commenced. Because of the long length of time these stars were observed, it is likely that we may discern flux variability over a long time period similar to our Sun’s magnetic cycle. Table 1 lists the positions and identifications of these sources. Table 2 shows their magnitudes in various wavelengths. Figure 4 illustrates each source’s position in the observed field.

2.1. Data Reduction

Chandra’s Interactive Analysis of Observations (CIAO) software version 4.6 (Fruscione et al. 2006) has been used to download and reprocess the *Chandra* X-ray data. The *XMM-Newton* data was reduced via the Science Analysis System (SAS) (Gabriel et al.

2006). We downloaded the files according to the observation identifications that correspond to *Chandra* and *XMM-Newton* observations (see Tables 3 and 4 for a list of all IDs). Because the CDFS contains stellar sources that are faint compared to the background noise, we decided not to subtract the background. When subtracted, the total flux during an epoch was a negative value. Apparently, there are certain time periods when the background counts are \geq the sources’ counts. The background spectra for observations in one epoch were averaged together. This is done so that we can have enough counts to ascertain an apt model for the background spectra and then fit the source spectra.

Spectra from multiple observations have been merged if the time interval between observations are merely a few months apart. We do not expect a significant change of magnetic activity pattern on this time scale. Consequently, some groups, or epochs, have a 7 month range while others are 2 months long. The epochs that individual observations were grouped to are shown in Tables 3 and 4. This grouping procedure provides more counts for the distinct spectra, which is essential for our faint stellar sources. We hope to discern variability between each epoch and find a cycle within the constraints of our data.

In this analysis data spikes caused by flares are not considered when searching for long-term cyclic activity. One type of solar flare that typically is read out by *Chandra* and *XMM-Newton* is the solar proton flare. Solar proton flares occur when highly energetic protons are emitted from the Sun. Even though *Chandra* and *XMM-Newton* instruments do not point toward the Sun, these protons are sufficiently energetic to penetrate the telescopes from any direction and reach the CCD detectors. Unfortunately, the detectors read these bombardments as X-ray photons. This event can cause the telescope to detect 1000 times more photons than it would detect without the solar proton flare. Typically, these detected events are evenly distributed on the CCDs. Consequently, the counts resulting from this flare type can be treated as part of the background. Solar proton flare counts can be deleted for the specific time span when the flare occurred. The counts from this flare are noticed when the counts dramatically increase for a (usually short) time interval. The counts spawned from this flare type were deleted early in the data reduction process. *Chandra* tends to defend itself from these solar proton flares better than *XMM-Newton*. As for a weak solar proton flare, CCDs read the counts from this as counts for the source and the background. If we encountered this circumstance we would have not deleted that time interval of data. In theory, having such a small increase of counts in the source and background would not have spawned any issues in our analysis. Lastly, there are flares that come from the actual point sources we observe and analyze. In this analysis we only care about the average X-ray luminosity. If an abnormally high group of flux values are detected within a time interval, the average of all fluxes except the abnormal values are considered to be the average flux of the star within that time scale.

2.2. Finding Optimal Spectral Fit

After averaging the spectra according to the epochs, the Sherpa software (Doe et al. 2007) was used to find

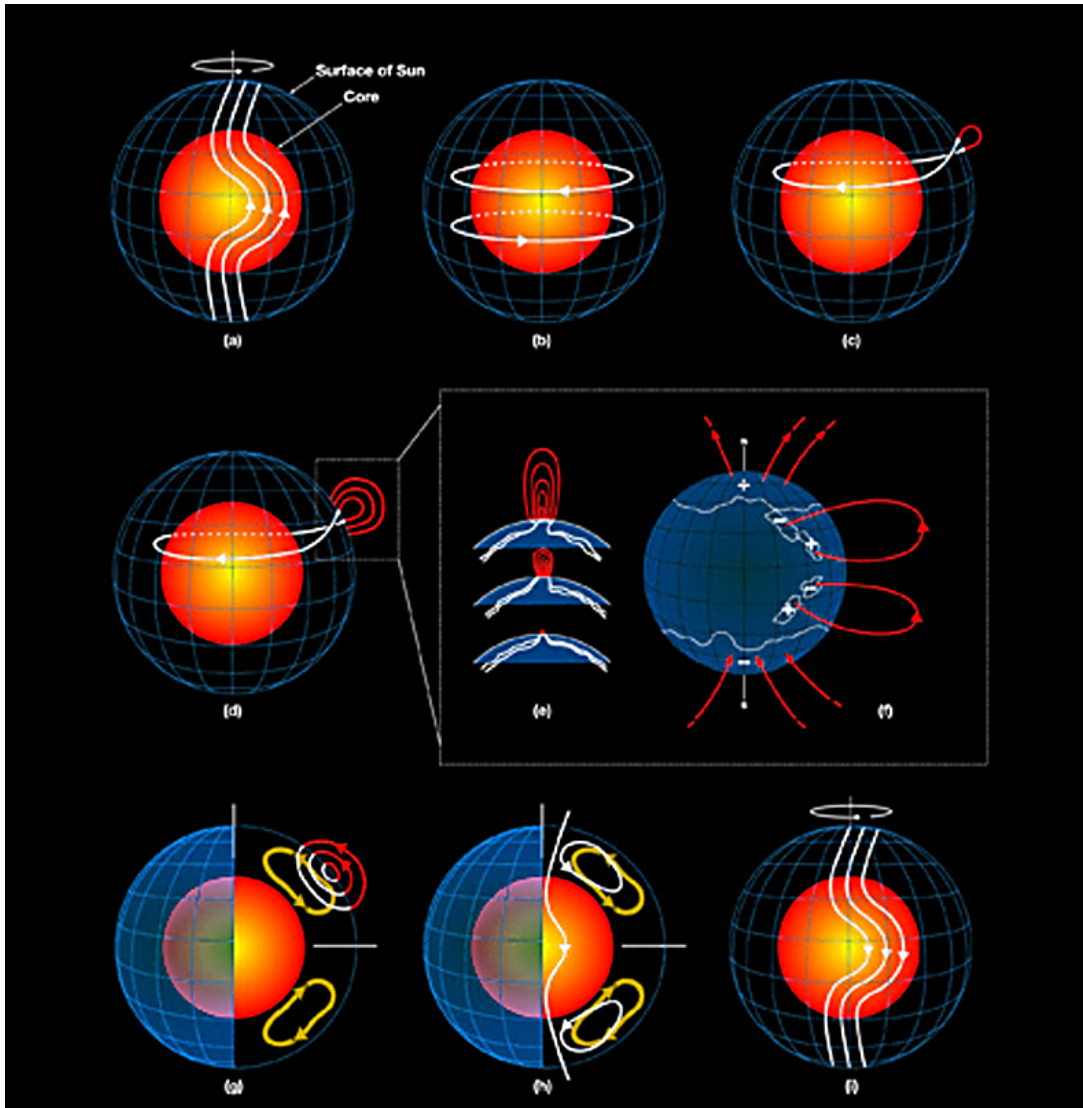


FIG. 1.—: Physical processes in the flux-transport dynamo that simulates and predicts solar cycles. (a) An initial poloidal magnetic field is transformed due to differential rotation. (b) The poloidal field becomes a toroidal field. (c) Magnetic flux rope emerges out of photosphere due to buoyancy instability below. (d) Several theories debatably explain how the flux rope rises as more magnetic field lines undergo reconnection around it. This part of the process represents years of activity as many coronal mass ejections (CMEs) and flares occur over time on a weekly basis. (e,f) There is a Mass Loading theory which describes the magnetic field as being stressed by the consistent subtraction of mass. As mass is lost in a CME, the sum of all forces is no longer zero and thus an eruption occurs (Low & Zhang 2002). The “breakout” model suggests that the magnetic field is sheared in the azimuthal plane, which causes an increase in magnetic pressure (Antiochos et al. 1999). The energy from the azimuthal component of the magnetic field is transferred to the non-azimuthal field. During this transfer, radial current sheets are formed and magnetic reconnection begins. The increase of gravitational energy, internal energy at the current sheets, and (primarily) kinetic energy compels the non-azimuthal energy to peak and subsequently decline. This rapid increase in kinetic energy constitutes the plasmoid eruption (MacNeice et al. 2004). Catastrophe models state that CME eruptions chronologically undergo stable, unstable, and stable equilibrium again. However, observations of CMEs seem to oppose the idea that the flux rope is in stable equilibrium at the end phase of a CME. As the flux rope rises during eruption, there is a point where a current sheet forms (Forbes & Priest 1995). Thus far solar observations seem to support the existence of current sheets (Savage et al. 2010). Due to the emergence of violent CMEs and flares, sunspots in photosphere and active regions in corona are formed. (g) Subsequently, magnetic reconnection occurs. (h) Tubes of magnetized fluid define the meridional component of the solar magnetic field. (i) A reversed poloidal magnetic field is regenerated and the ~ 11 year sunspot cycle repeats (Charbonneau 2010).

a satisfactory model to describe our source and background data distinctly. The APEC (Foster et al. 2012) model we used accounts for the characteristics of an optically thin coronal plasma system. Coronae emit X-rays mostly in the 0.3-7.0 keV bands that we consider in this analysis. The source model that we initially used to fit our stellar spectra is described as *xsphabs*xapec*. The “xs” before the model name signifies that it is derived by XSPEC software (Arnaud 1996). The “phabs”, or photo-electric absorption, model is described in Equa-

tion 1. The APEC model contains four parameters: the plasma temperature in keV, the redshift, the normalization, and the abundances for metals and other elements such as C, N, O, Ne, Mg, Al, Si, S, Ar, Ca, Fe, and Ni (with He fixed at cosmic). The normalization is presented in Equation 2 (Doe et al. 2007).

$$M(E) = e^{(-N_h * \sigma(E))} \quad (1)$$

The $M(E)$ is the photo-electric absorption, the $\sigma(E)$ is the photo-electric cross-section that does not include

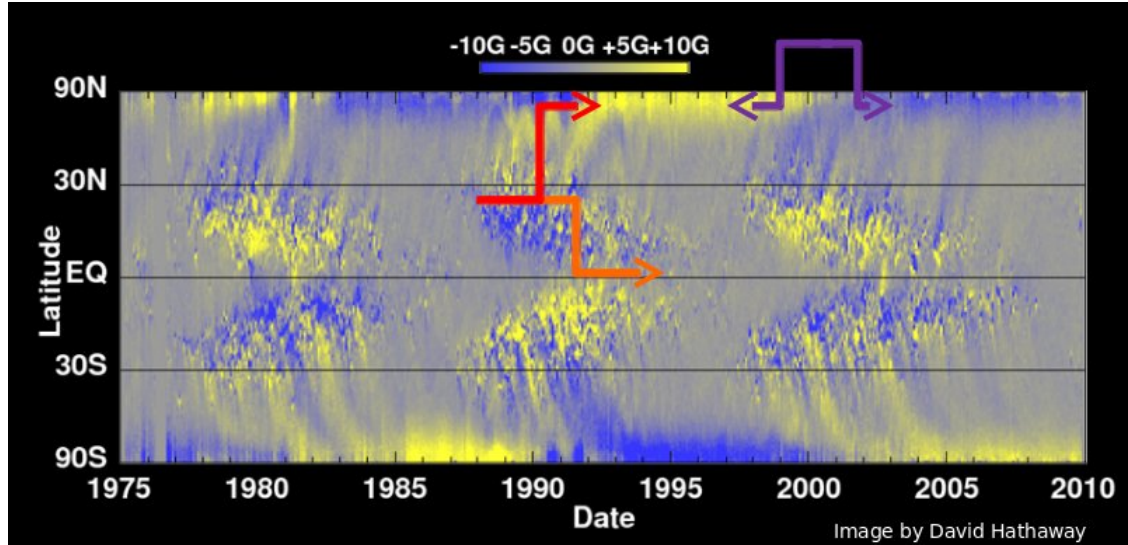


FIG. 2.—: A synoptic magnetogram displaying the migration of active regions toward the equator. **Bottom arrow:** Active regions tend to emerge at 30° latitude and move towards equator over the course of ~ 11 years. **Top left arrow:** Magnetic flux is released from decaying sunspots and migrates to the poles. **Top right arrow:** Polar field reversal is observed at the peak of the sunspot cycle (Hathaway 2014, <http://solarscience.msfc.nasa.gov/images/magfly.jpg>).

DAILY SUNSPOT AREA AVERAGED OVER INDIVIDUAL SOLAR ROTATIONS

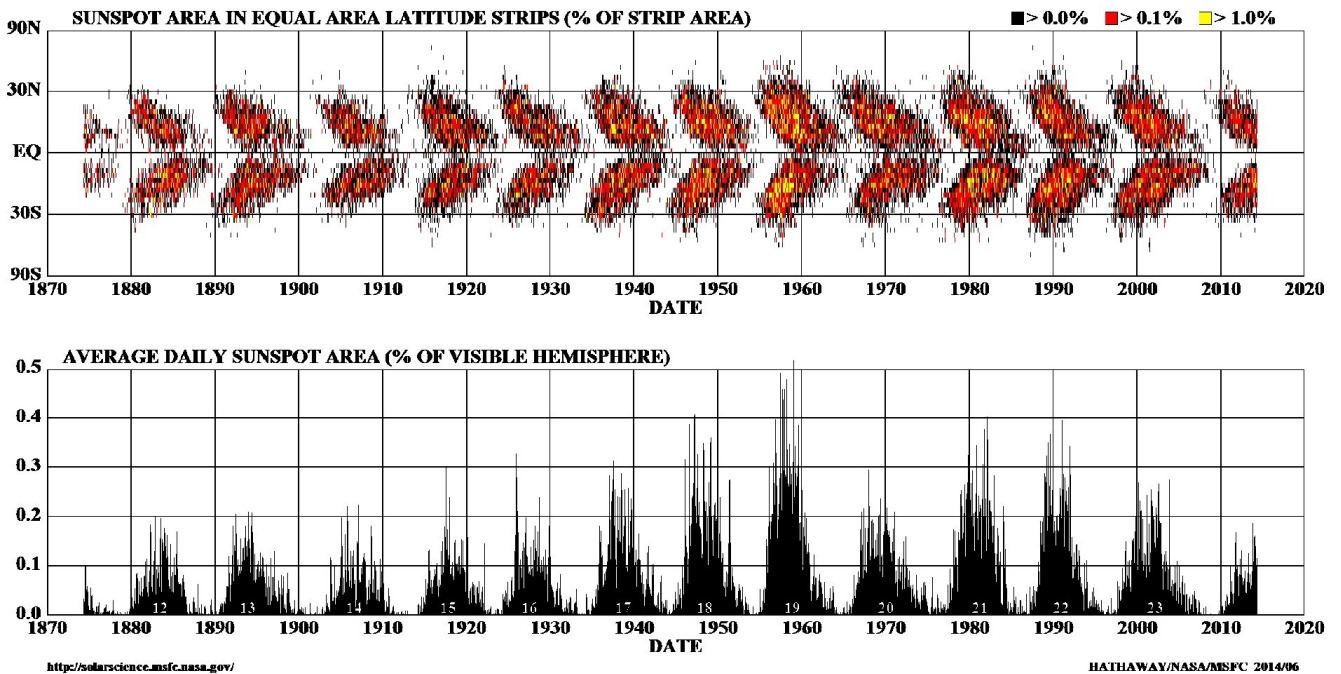


FIG. 3.—: The first graph is a “butterfly” diagram illustrating the equatorward migration of active regions. The end of one sunspot cycle overlaps with the beginning of another. The second graph shows the fraction of area covered on a hemisphere by the sunspots over time. (Hathaway 2014, <http://solarscience.msfc.nasa.gov/images/bfly.gif>).

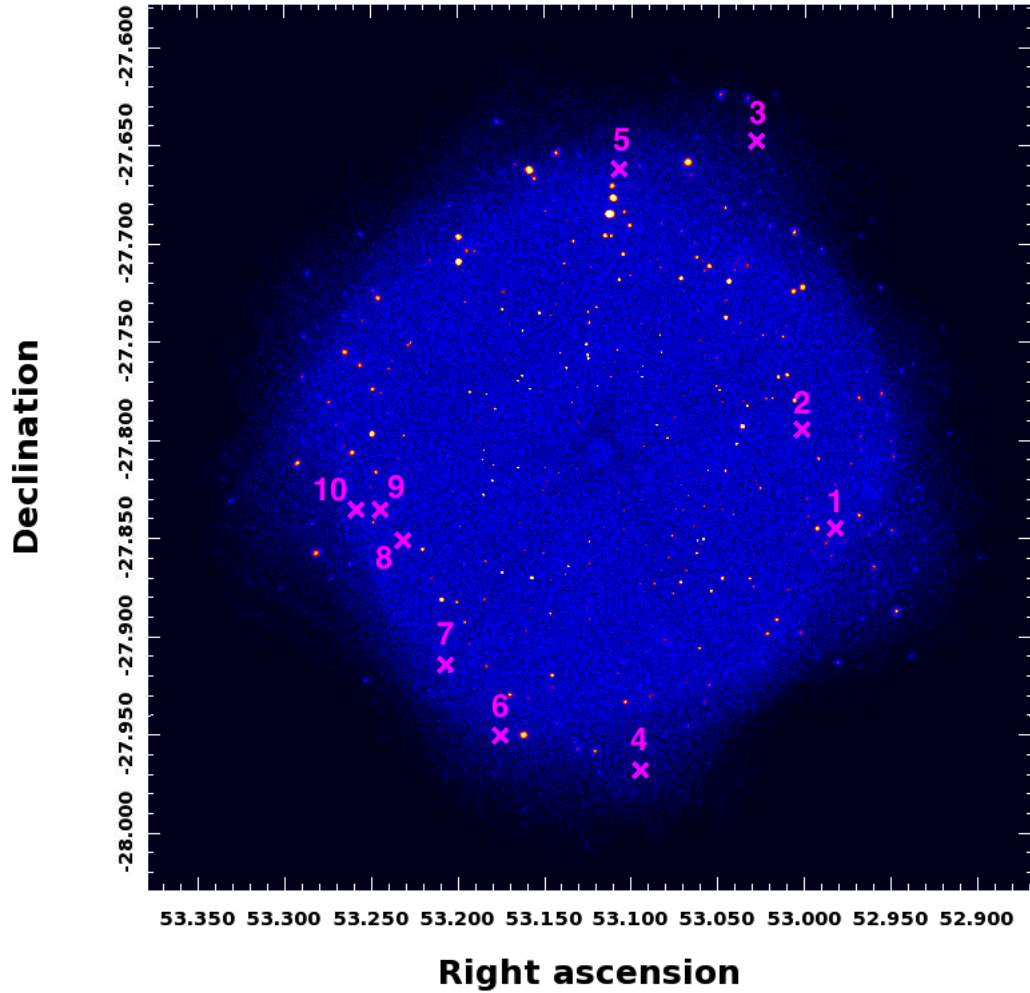


FIG. 4.—: Exposure corrected mosaic image of 56 Chandra deep field south observations. This image covers an energy range of 0.5 - 6.0 keV and only the ACIS-I (ccd id = 0-3) detector of Chandra. The total exposure time of this image is 3.8Ms. The magenta crosses correspond to the sources listed in Tables 1-4 that we will analyze. In this analysis, we decided that the 5th source was too faint to obtain a good quality spectral fit.

Thomson scattering. The N_h is the equivalent hydrogen column (in units of 10^{22} atoms/cm²).

$$\frac{10^{-14}}{4\pi(D_A * (1 + z))^2} \int n_e n_h dV \quad (2)$$

The D_A is the distance (in cm) to the source, z is the redshift, n_e is the electron density (in cm⁻³), and n_h is the hydrogen density (in cm⁻³).

2.2.1. Background Model

As stated previously, we have faint sources that sometimes do not provide more counts than the background noise. When we subtracted the background from each observation initially, there were few counts remaining. Consequently, we tried fitting the spectra without subtracting the background. The Cash statistic (Cash 1979) provided the fit results. The source model *xspfabs*xsapec* did not fit well with the data. The plasma temperature value was consistently over 5 keV when we know that typically X-ray coronal sources should be around 2 keV. Afterwards, we decided to temporarily analyze only the background spectra to find a good background model. We then combined the spectra for background regions of all epochs for one source at a time. This gave us more counts to analyze in the spectra. From here on throughout the analysis, we used the χ^2 statistic with a Gehrels variance function to evaluate the confidence. After attempting to fit the background with Sherpa's constant function ("const1d") and powerlaw function ("powlaw1d"), we learned that a model described as *powlaw1d+const1d* provided the best fit results for the background. Subsequently, we tested this model when we combined the background spectra of all sources for one epoch at a time. This strategy resulted in a better background fit. Figure 6 shows one result of this. Figure 7 illustrates the same background model fitted to the same source during a different epoch of observations. Unfortunately, the spectra show a spike in the data around the 2.1-2.3 keV band due to gold emission from the detector. We determined that this is not a large problem because we can ignore that small region without losing much signal.

After we seemed to get a reasonable background fit, we fitted the source spectra again. Within most of the energy range 0.3-7.0 keV, the fit was satisfactory. However, we needed to ameliorate the fit in the 0.3-1.0 keV range. It seemed as if the background model's powerlaw function was not accounting for the counts in that range as well as we thought it would. Due to this, we tried to fit (only) the background within solely the 0.3-1.0 keV range, as shown in Figure 8. When we seemed to have found the model for best fit, we used the values in those fit results as frozen parameter values for the background model when we fitted the source (and background) spectra again. Figure 9 displays this result.

2.2.2. Satisfactory Spectral Fit

We focused on the background intently because we considered that there may be additional X-ray emission detected that our simplest models did not account for. After many trials, we have concluded that this idea is unlikely. Furthermore, we found that the best model for the background seems to be the constant function

alone. This deduction may seem contrary to our ideas previously stated; however, the constant function fits well with our data throughout energy bands 0.3-7.0 keV *only* when the function of the Auxiliary Response File (ARF) did not fold the constant function (background model). At very soft energy bands (~ 0.5 keV) the ARF would account for the low efficiency of *Chandra* to detect very soft X-rays. This caused the background model to not fit well in those energy bands, as seen in Figure 9. Nevertheless, the ARF was not tampered with in regards to the source model *xspfabs*xsapec*. The consequent improved fit is shown in the higher plot of Figure 10. This improvement taught us that the absorption component of our model may not be as significant to include as we initially thought. We then attempted to ameliorate the source model again by using two *xsapec* functions with no absorption function. The lower spectrum in Figure 10 shows a better fit than the first plot because of this. The enhanced fit was primarily due to the use of two temperature parameters, rather than one. After this trial, we wanted to see if the best models we used would fit well to the data when the spectra were only averaged by epochs. Figures 8-10 displayed fits for the averaged spectra of all sources (only to experiment with various models) or for the spectra averaged throughout all observations for each source. The latter was most beneficial and provided us with sufficient counts to confidently rely on χ^2 statistics to determine the confidence of our spectral fits. Once we found the model that seemed to best fit our data, we attempted to fit the averaged spectra of observations solely within each epoch. Unfortunately, we determined that the *Chandra* data did not provide enough counts for us to obtain a good fit for its spectra. We then analyzed the *XMM-Newton* spectra in which we knew would provide plenty of counts.

Initially, we subtracted the background in the *XMM-Newton* data because we had sufficient counts to do so. After several trials, we found that the best source model (in this case) utilized only an *xsapec* function. Due to our abundance of counts, this was easily done for the averaged spectra of each epoch. χ^2 statistics determined the confidence of all our *XMM-Newton* spectral fits. Subsequently, we made spectral fits that did not have the background subtracted. In this case, the *powlaw1d+const1d* provided the best fit for the background. The one *xsapec* function remained as the best source model. The spectral fits with background counts were significantly, although not substantially, better than the fits with background subtracted data, as Figure 11 illustrates.

2.3. The Lomb-Scargle Periodogram

Flux values for four sources have been computed for each epoch by integrating the APEC model in the energy range 0.3-7.0 keV. The consequent light curves will be examined for the existence of periodic behavior via the Lomb-Scargle periodogram (LSP) (Lomb 1976; Scargle 1982). The peak frequency and the strongest periodicity found from the "false alarm probability" (FAP) will be yielded from the LSP. The peak frequency is the best-fit sinusoidal function for the data, and the FAP is the probability that periodic behavior of a specific magnitude could be found in Gaussian noise.

3. DISCUSSION

Four light curves are presented for the four brightest sources (see Figure 5). The effect of analyzing such faint sources is illustrated in the error bars. Some of the large errors are due to few observations (with exposure times of ~ 10 ks) within certain epochs. In all four light curves, the *XMM-Newton* fluxes have smaller error bars than the *Chandra* fluxes. As stated previously, the *XMM-Newton* data provided much more counts than *Chandra*, and thus the spectral fits for the *XMM-Newton* data provided stricter constraints than for the *Chandra* data. Nonetheless, valuable information can be extracted from the light curves in regards to the sources' long term variability.

None of our sources seem to exhibit flux variability of a factor ~ 10 like the Sun. The flux of source #4 seems to remain constant throughout the observations. There is a lack of data between 2002 and 2008. Moreover, the one data point within that time period is associated with a large error value. Therefore, we are not certain if the stellar corona truly remained constant throughout these years. However, we are confident that the flux variability did not exceed a factor of 3. Source #6 certainly expresses flux variability, although this does not seem to be periodic. We are not sure if this is a sign of long-term variability. This is the brightest source out of the nine selected (although still faint). Its brightness allowed a good spectral fit, which resulted in the relatively small errors associated with its flux values. There is an excessive time span (near 2002 to 2008) in which there were no observations of this source. The flux variability does seem to reach a factor of 2 if we assume its quiescent flux is $\sim 7 \times 10^{-15} \frac{\text{erg}}{\text{s-cm}^2}$. Source #7 unfortunately has relatively large errors for every point on the light curve. Its flux seems to remain constant throughout all epochs. The flux of source #9 also seems to remain quiescent throughout the epochs. However, like the other light curves, we cannot confidently conclude that it is not an active star. Among other obvious reasons, this lack of confidence is due to a ~ 6 year gap in our data.

4. CONCLUSIONS

For this analysis, we utilized CIAO and SAS to download and reprocess the data for nine point sources observed within the CDFS. Although faint, these sources were useful to analyze due to their frequent appearance within the *Chandra* and *XMM-Newton* observations across a period of ~ 11 years. The lack of photons detected (for the point sources) significantly decreased the feasibility of obtaining good quality spectral fits. We find that an APEC model comprised of merely one function known as *xsapec* (in Sherpa) sufficed in describing our stellar sources. We neglected the ARF only in regards to the background obtained from the *Chandra* observations. The *Chandra* background spectra were low in counts primarily due to the small background regions used to extract the spectra. The background regions needed to be small because of the many dispersed sources (point and extended) within the field observed. Consequently, the *Chandra* spectral fits were not satisfactory. However, the *XMM-Newton* spectral fits were satisfactory but the small amount of epochs used for our light curves hindered us from confidently concluding whether or not our

four brightest sources exhibited long-term flux variability similar to the Sun. Source #6 seems to be the best candidate within our nine star sample for possibly having a long-term coronal cycle. However, we do conclude that none of the four sources express a long-term variability above a factor of 3. This analysis attests to the difficulty of conclusively discovering long-term X-ray coronal cycles without the initial aid of Ca II H and K emission information from the stellar chromospheres.

5. ACKNOWLEDGEMENTS

It was a privilege to collaborate with such ingenious advisors at the Harvard-Smithsonian Center for Astrophysics. I am grateful to Katja Poppenhaeger for her guidance as it was needed during my primary advisor's short absence. I thank Nick Wright for answering my inquiries and downloading much of data for me. I appreciate the time Johnathan McDowell spent to assist me in resolving a variety of problems throughout this research. I thank Marie Machacek for her unwavering support, encouragement, and wise advice that was always given with enthusiasm. It was my pleasure to be surrounded by Astronomy REU interns who were always eager to help and share their knowledge with me: Christopher Capiello, Virginia Cunningham, Kirsten Blancato, Allison Matthews, Zhoujian Zhang, Lee Rosenthal, Zequan Li, Nicole Melso, Peter Senchyna, and Catherine Zucker. This research has made use of data obtained from the Chandra Data Archive and the Chandra Source Catalog, and software provided by the Chandra X-ray Center (CXC) in the application packages CIAO, ChIPS, and Sherpa. This work is supported in part by the National Science Foundation REU and Department of Defense AS-SURE programs under NSF Grant no. 1262851 and by the Smithsonian Institution.

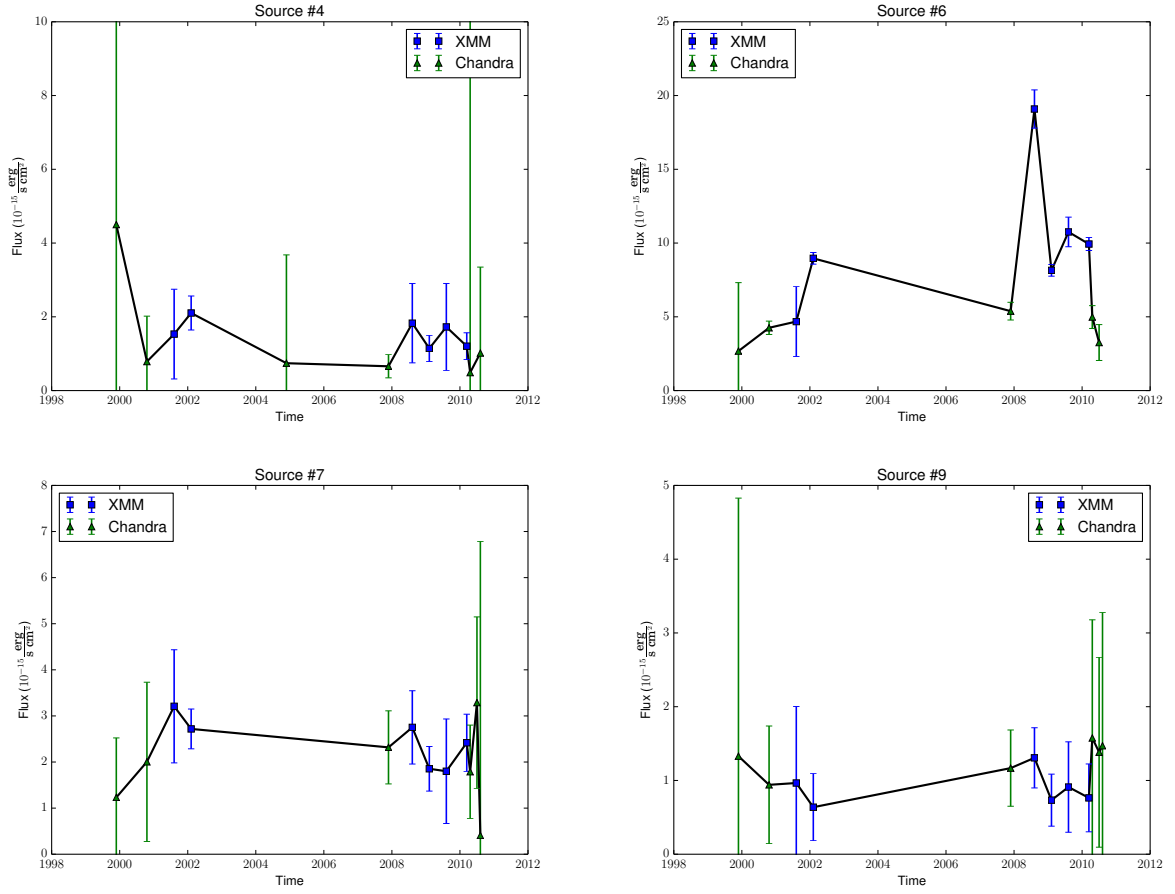


FIG. 5.—: Four light curves are presented. Refer to Tables 1-4 for information about the sources and observations.

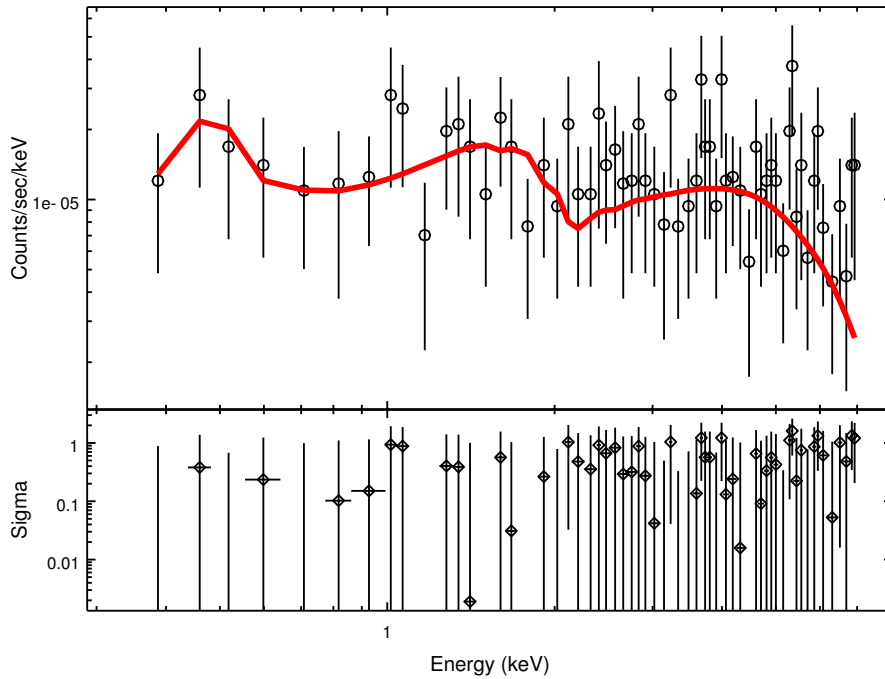


FIG. 6.—: Spectra of background region for source #6 during epoch 2010 (05-06) (refer to Tables 1 and 3). This background spectrum was fitted with the model $powlaw1d+const1d$. This was better than fitting it with only a powerlaw function or only a constant function.

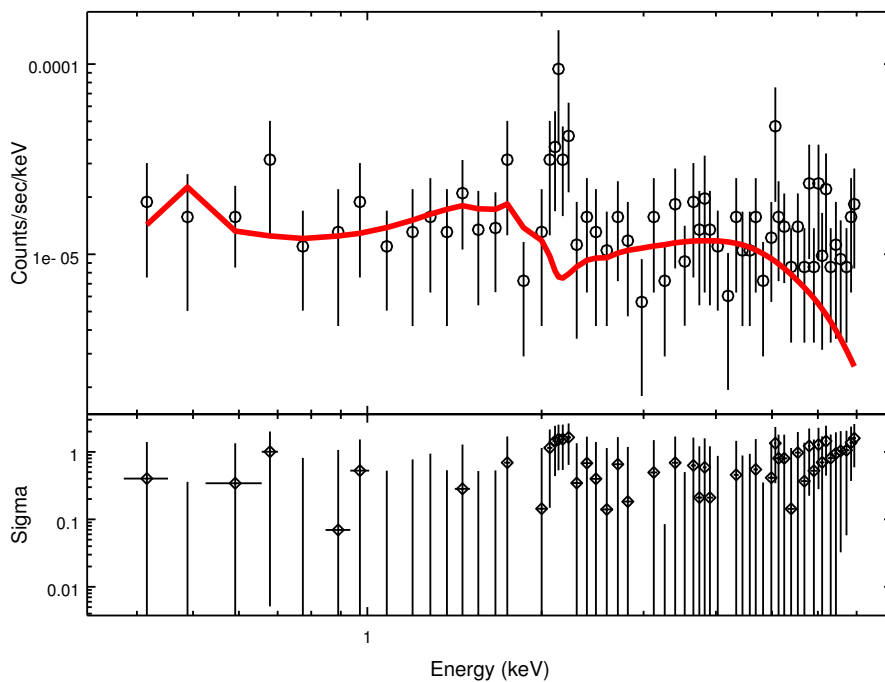


FIG. 7.—: Spectra of background region for source #6 during epoch 2007 (refer to Tables 1 and 3). There is a spike in the 2.1-2.3 keV range within the source and background data due to fluorescent X-ray emission from gold on the *Chandra* ACIS-I detector.

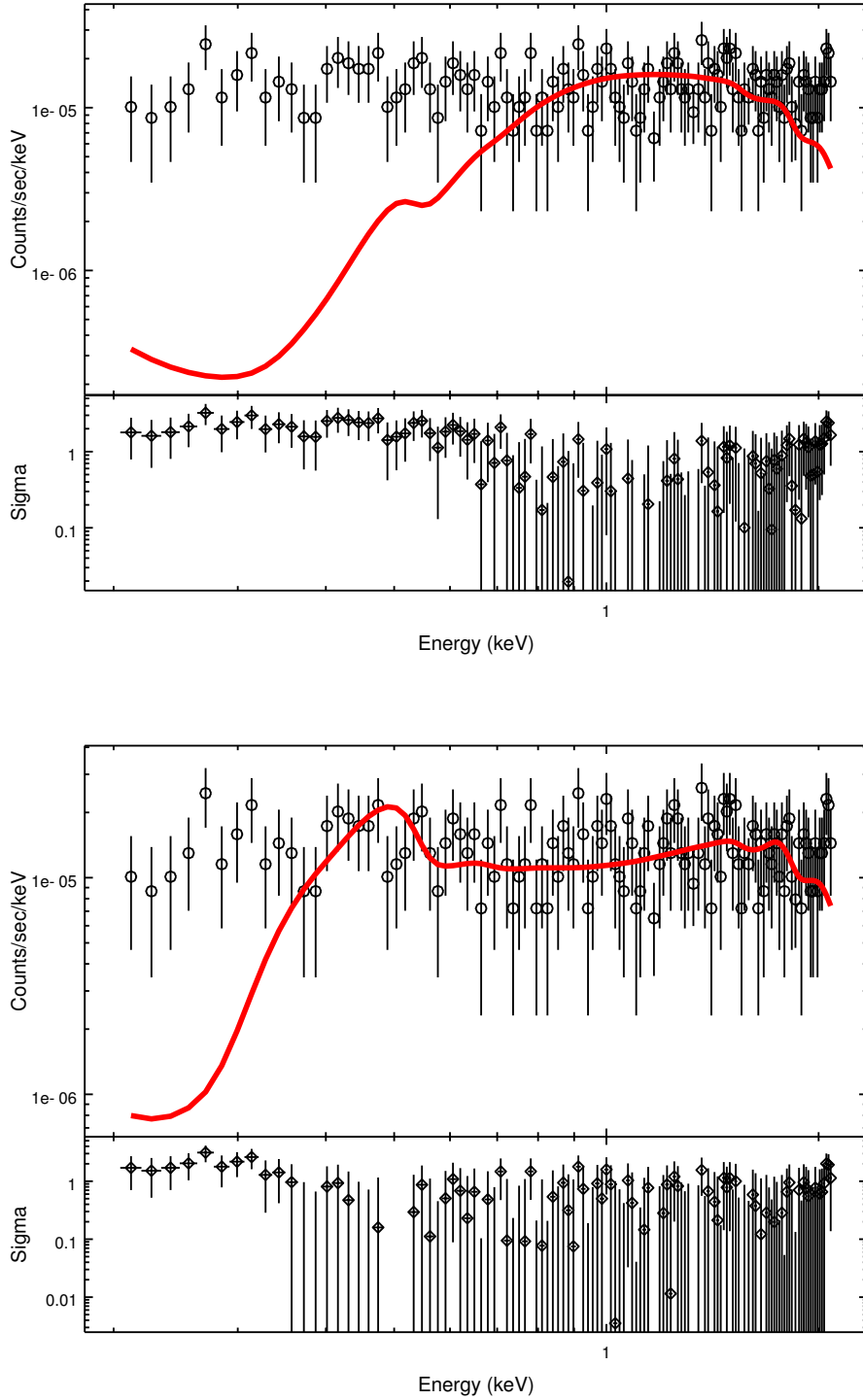


FIG. 8.—: Averaged spectra for background regions of all sources during epoch 2007 (refer to Table 3).

Top plot: Spectral fit with only a powerlaw function as the model.

Bottom plot: A better fit is seen because a constant function was added to the powerlaw.

It is clear that our model did not fit the very low energy bands well. Figure 10 explains and illustrates how the fit was ameliorated in the energy bands < 0.6 keV.

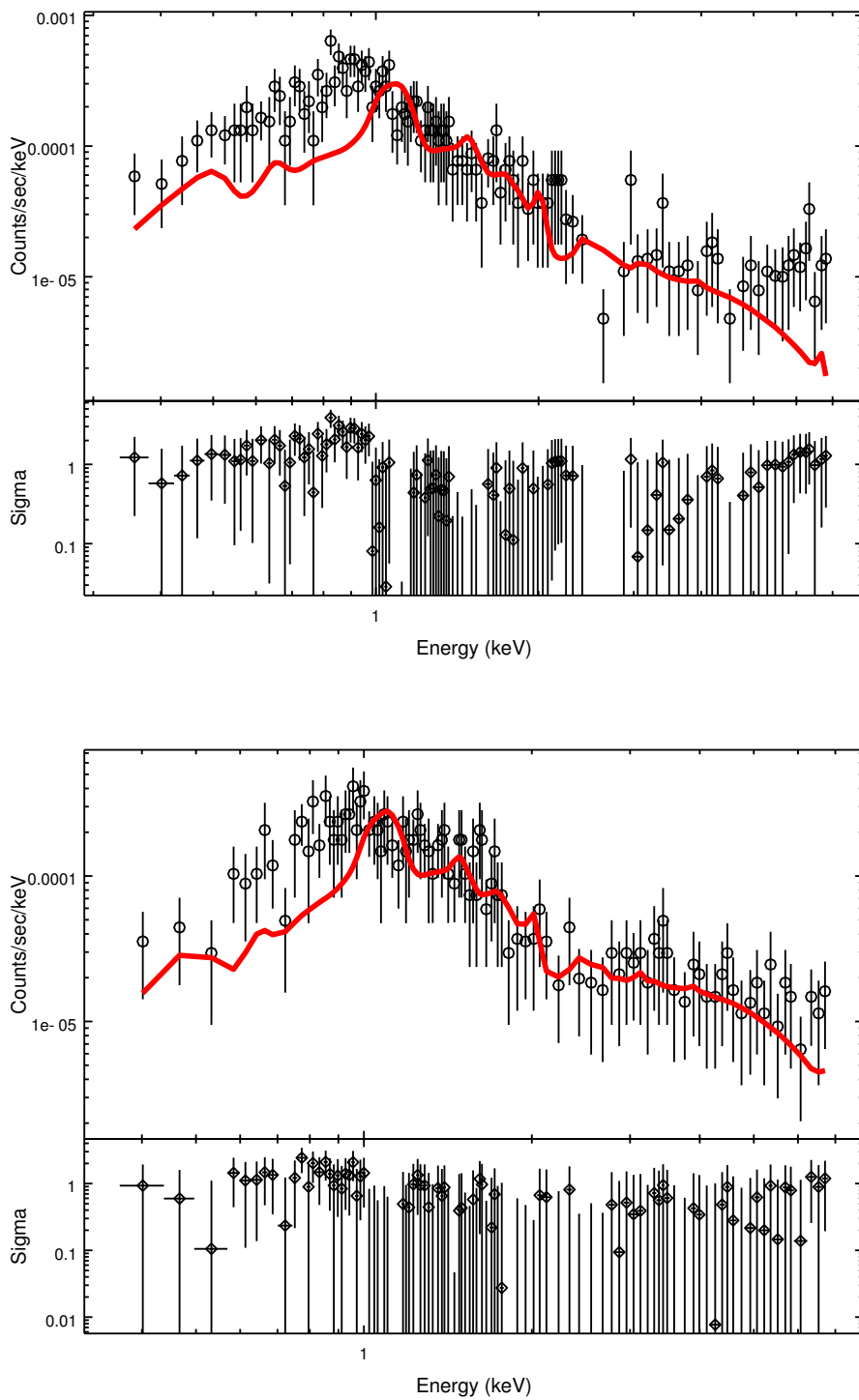


FIG. 9.—: Both plots are distinct examples of the results gained when the $xsphabs*xsapec$ model describes the source while the $powlaw1d+const1d$ model (which contained frozen parameters) describes the background.
 Top plot: Averaged spectra of all sources during epoch 2000.
 Bottom plot: Averaged spectra of all sources during epoch 2010 (05-06) (refer to Table 3).

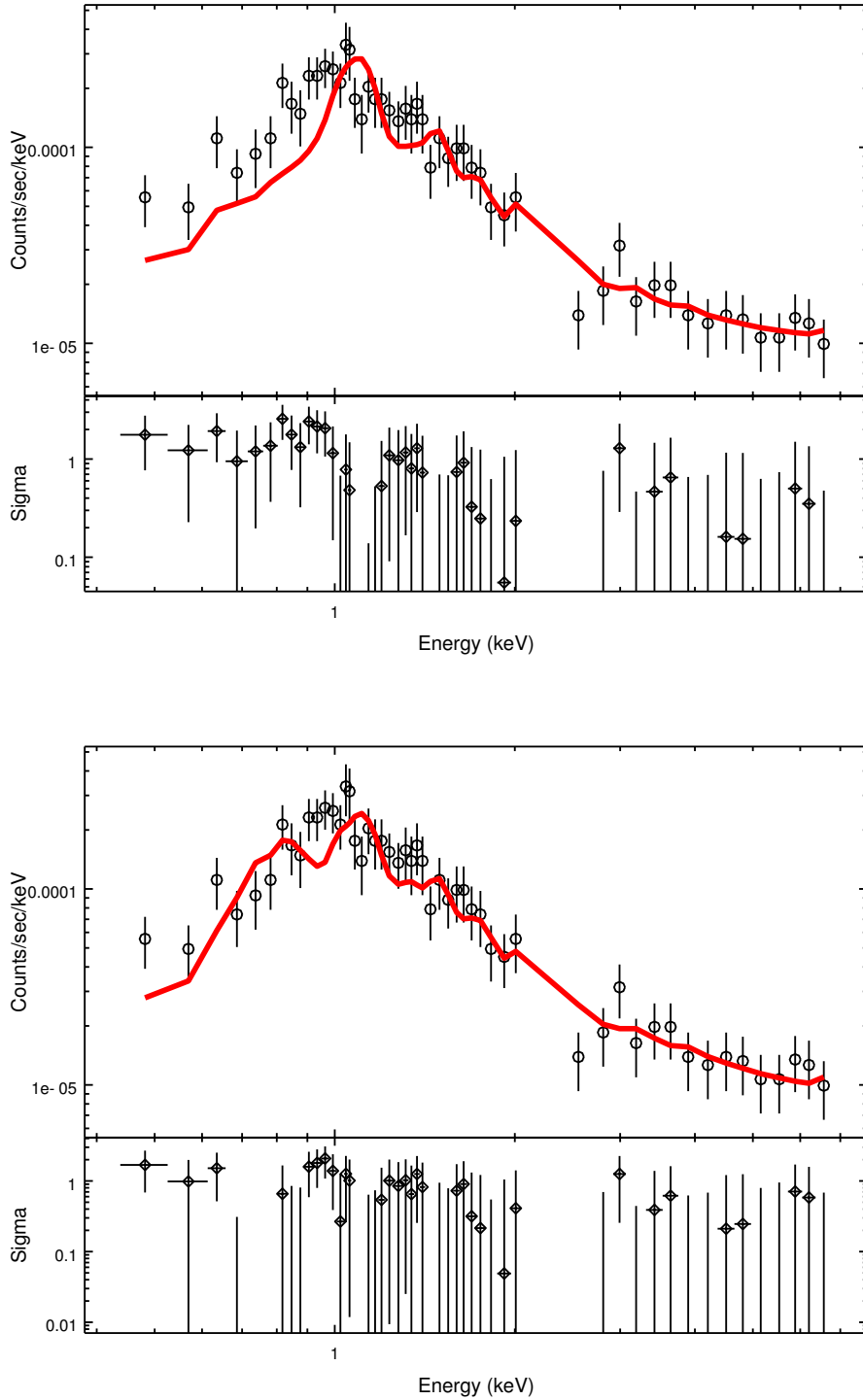


FIG. 10.—: Averaged spectra of source #7 for all observations (refer to Table 1). The energy range (2.1-2.3 keV) where the data spike was found, previously emphasized in Figure 7, is no longer considered.

Top plot: The source model $xsphabs*xsapec$ was used. We neglected the ARF for the background spectrum. The constant function model ($const1d$) sufficed to fit the background data well. It seems that ARF reduction is a better strategy than modeling the background with an additional powerlaw, as previously shown in Figure 9.

Bottom plot: Again, we neglected the ARF for the background. The model for this fit was $xsapec+xsapec$.

We benefitted primarily from the use of two temperature parameters instead of one. The two temperatures are near 2 keV and 0.5 keV.

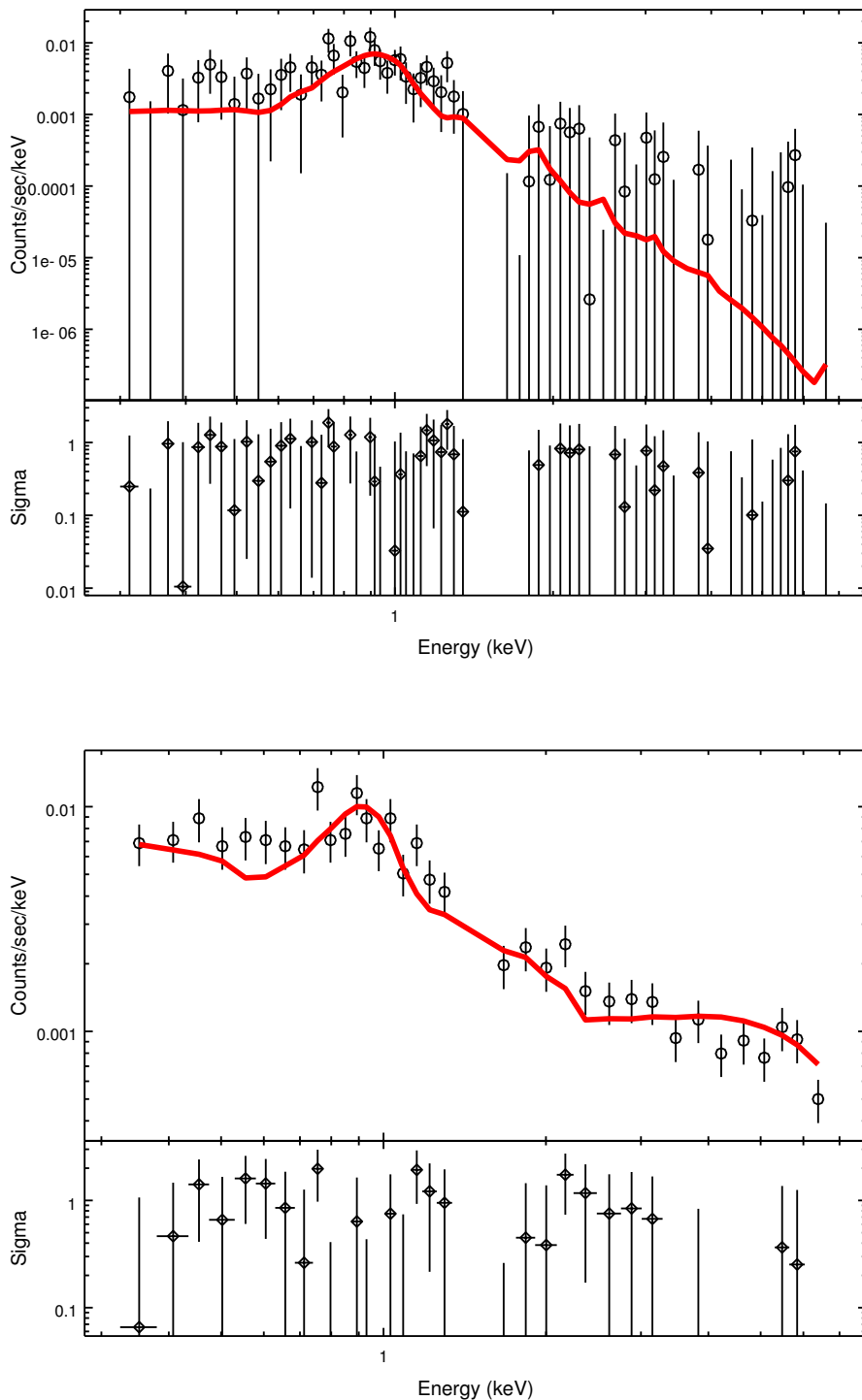


FIG. 11.—: Averaged spectra of source #7 for all observations of epoch 6 observed by *XMM-Newton* (refer to Tables 1 and 4).

All spectra for *XMM-Newton* contained a data spike from 1.40 to 1.55 keV, which was ignored. For epochs 4 and 6, there was additional emission from 5.75 to 6.0 keV. This energy range also had to be ignored. The spikes were caused by Al K and Si K line fluorescent X-ray emission from *XMM-Newton* detectors.

Top plot: One *xsapec* function comprised the model for this background subtracted spectral fit.

Bottom plot: The source was fitted with the same model. The background model was described as *powlaw1d+const1d*. For virtually every source and each epoch, the source and background data fits yielded better results than when the background was subtracted.

APPENDIX

TABLE 1: Identities

Source #	RA	Dec	Catalog	Catalog ID	CDFSH ID ³	Stellarity Index ³	Class ^{1*}	Spectral Type ⁴
1	03:31:55.56	-27:50:43.60	CXOYECDF ⁵	J033155.5-275045	2815	1	Star	MSM4V
2	03:32:00.30	-27:47:42.40	2MASS ⁶	J03320029-2747427	1729	1	...	MSM0III
3	03:32:06.66	-27:38:52.00	CXOYECDF ⁵	J033206.7-273852	151	0.99	Star	MSM4V
4	03:32:22.56	-27:58:05.30	CXOECDFS ⁷	J033222.4-275804	4413	0.97
6	03:32:42.02	-27:57:02.40	CXOYECDF ⁵	J033242.0-275702	4540	1	Star	...
7	03:32:49.66	-27:54:54.10	CXOYECDF ⁵	J033249.6-275454	4008	1	Star	MSK0V
8	03:32:55.51	-27:51:06.20	GOODS ⁸	J033255.5-275106	3471	0.99	Star	...
9	03:32:58.54	-27:50:07.70	CXOYECDF ⁵	J033258.5-275007	3353	0.99	Star	MSM3V
10	03:33:01.84	-27:50:09.50	CXOCDFS ⁹	J033301.9-275009	3375	0.98	...	MSM2.5V

* Because these sources are faint, few people have observed and/or analyzed them. Ellipses are seen because these sources have not been classified in the literature. It has also been difficult to find some of their magnitudes, as Table 2 shows. See the footnotes at the bottom of this page for the references corresponding to the information (assigned with numerical superscripts) in this table.

TABLE 2: Magnitudes:

Source #	R ¹	Error R ¹	U ²	Error U ²	H ³	Error H ³	B ⁴	Error B ⁴	V ⁴	Error V ⁴	I ⁴	Error I ⁴
1	19.71	0	23.39	0.06	16.12	0.003	22.04	0.01	20.91	0.01	17.78	0
2	16.86	0	20.38	0.01	14.38	0.001	18.91	0	17.93	0	15.86	0
3	18.83	0	22.37	0.02	15.28	0.002	21.15	0	20.04	0	16.82	0
4	13.95	0.01	13.35	0	10.03	0	14.46	0.01	14.1	0.01	13.62	0.01
6	17.6	0	10.79	0
7	17.81	0	14.2	0.001	16.66	0	16.16	0	15.15	0
8	15.6	0	13.41	0
9	17.38	0	21.86	0	14.06	0.001	19.7	0	18.56	0	15.7	0
10	18.45	0	22.1	0.02	15.4	0.001	20.69	0	19.61	0	16.96	0

These measurements are in the AB astronomical magnitude system. This system is based on flux measurements that were calibrated in absolute units.

¹(Silverman et al. 2010)

²(Luo et al. 2010)

³(Moy et al. 2003)

⁴(Groenewegen et al. 2002)

⁵(Virani et al. 2006)

⁶(Cutri et al. 2003)

⁷(Lehmer et al. 2005)

⁸(Giavalisco et al. 2004)

⁹(Giacconi et al. 2002)

TABLE 3: Epochs: *Chandra*

Year Month	1999 (10-11)	2000 (05-12)	2004 (11)	2007 (09-11)	2010 (03-04)	2010 (05-06)	2010 (07)
	1431-0	441	5020	8591	12043	12055	12053
	1431-1	582	5019	9593	12123	12213	12054
		2406		9718	12044	12048	12230
		2405		8593	12128	12049	12231
		2312		8597	12045	12050	12227
		1672		8595	12129	12222	12233
		2409		8592	12135	12219	12232
		2313		8596	12046	12051	12234
		2239		9575	12047	12218	
				9578	12137	12223	
				8594	12138	12052	
				9596		12220	

Observation identifications are listed in epochs comprised of observations that occurred within relatively short time periods of each other.

TABLE 4: Epochs: *XMM-Newton*

Year Month	2001 (07)	2002 (01)	2008 (07)	2009 (01)	2009 (07)	2010 (01-02)
	0108060401	0108060601	0555780101	0555780501	0604960101	0604960501
	0108060501	0108060701	0555780201	0555780601	0604960201	0604960601
		0108061801	0555780301	0555780801	0604960301	0604960701
		0108061901	0555780401	0555780901	0604960401	0604960801
		0108062101		0555781001		0604960901
		0108062301		0555781701		0604961001
				0555781901		0604961101
				0555782001		0604961201
				0555782101		0604961301
				0555782201		0604961801
				0555782301		
				0555782401		

Observation IDs are shown for the observations that we used within these epochs.

REFERENCES

- Antiochos, S. K., DeVore, C. R., & Klimchuk, J. A. 1999, *ApJ*, 510, 485
- Arnaud, K. A. 1996, in *Astronomical Society of the Pacific Conference Series*, Vol. 101, *Astronomical Data Analysis Software and Systems V*, ed. G. H. Jacoby & J. Barnes, 17
- Ayres, T. R. 2009, *ApJ*, 696, 1931
- Ayres, T. R., Judge, P. G., Saar, S. H., & Schmitt, J. H. M. M. 2008, *ApJ*, 678, L121
- Baliunas, S. L., Donahue, R. A., Soon, W. H., et al. 1995, *ApJ*, 438, 269
- Cash, W. 1979, *ApJ*, 228, 939
- Charbonneau, P. 2010, *Living Reviews in Solar Physics*, 7, 3
- Cutri, R. M., Skrutskie, M. F., van Dyk, S., et al. 2003, *VizieR Online Data Catalog*, 2246, 0
- Doe, S., Nguyen, D., Stawarz, C., et al. 2007, in *Astronomical Society of the Pacific Conference Series*, Vol. 376, *Astronomical Data Analysis Software and Systems XVI*, ed. R. A. Shaw, F. Hill, & D. J. Bell, 543
- Favata, F., Micela, G., Orlando, S., et al. 2008, *A&A*, 490, 1121
- Forbes, T. G., & Priest, E. R. 1995, *ApJ*, 446, 377
- Foster, A. R., Ji, L., Smith, R. K., & Brickhouse, N. S. 2012, *ApJ*, 756, 128
- Fruscione, A., McDowell, J. C., Allen, G. E., et al. 2006, in *Society of Photo-Optical Instrumentation Engineers (SPIE) Conference Series*, Vol. 6270, *Society of Photo-Optical Instrumentation Engineers (SPIE) Conference Series*
- Gabriel, C., Guainazzi, M., & Metcalfe, L. 2006, *Ap&SS*, 305, 315
- Giacconi, R., Zirm, A., Wang, J., et al. 2002, *ApJS*, 139, 369
- Giavalisco, M., Ferguson, H. C., Koekemoer, A. M., et al. 2004, *ApJ*, 600, L93
- Groenewegen, M. A. T., Girardi, L., Hatziminaoglou, E., et al. 2002, *A&A*, 392, 741
- Hale, G. E. 1908, *ApJ*, 28, 315
- Hempelmann, A., Robrade, J., Schmitt, J. H. M. M., et al. 2006, *A&A*, 460, 261
- Lehmer, B. D., Brandt, W. N., Alexander, D. M., et al. 2005, *ApJS*, 161, 21
- Lomb, N. R. 1976, *Ap&SS*, 39, 447
- Low, B. C., & Zhang, M. 2002, *ApJ*, 564, L53
- Luo, B., Brandt, W. N., Xue, Y. Q., et al. 2010, *ApJS*, 187, 560
- MacNeice, P., Antiochos, S. K., Phillips, A., et al. 2004, *ApJ*, 614, 1028
- Moy, E., Barmby, P., Rigopoulou, D., et al. 2003, *A&A*, 403, 493
- Robrade, J., Schmitt, J. H. M. M., & Favata, F. 2005, *A&A*, 442, 315
- Savage, S. L., McKenzie, D. E., Reeves, K. K., Forbes, T. G., & Longcope, D. W. 2010, *ApJ*, 722, 329
- Scargle, J. D. 1982, *ApJ*, 263, 835
- Schwabe, M. 1843, *Astronomische Nachrichten*, 20, 283
- Silverman, J. D., Mainieri, V., Salvato, M., et al. 2010, *ApJS*, 191, 124
- Virani, S. N., Treister, E., Urry, C. M., & Gawiser, E. 2006, *AJ*, 131, 2373
- Wilson, O. C. 1968, *ApJ*, 153, 221
- . 1978, *ApJ*, 226, 379